CrossMark

Pulsed sonication for alumina coatings on high-capacity oxides: Performance in lithium-ion cells

Vilas G. Pol [a,c], Yan Li [a,b], Fulya Dogan [a], Ethan Secor [a], Michael M. Thackeray [a], Daniel P. Abraham [a,*]

[a] Argonne National Laboratory, 9700 S. Cass Avenue, Argonne, IL 60439, USA
[b] Materials Science Program, University of Rochester, Rochester, NY 14627, USA
[c] School of Chemical Engineering, Purdue University, West Lafayette, IN 47907, USA

HIGHLIGHTS

- Pulsed-sonication is a rapid and effective approach for coating alumina on oxides.
- Oxide integrity and morphology is maintained after the coating process.
- NMR data indicate that octahedral Al bound to oxygen is contained in the coating.
- Cells with the alumina-coated particles shower better performance retention.

ARTICLE INFO

ABSTRACT

High-capacity xLi$_2$MnO$_3$·$(1 - x)$LiMO$_2$ (M = Ni, Mn, Co) oxides show relatively rapid performance degradation when cycled at voltages >4.5 V vs. Li/Li$^+$. Previous research has indicated that modifying the oxide surfaces with coatings, such as alumina, reduces cell impedance rise and improves capacity retention. In this article, we demonstrate pulsed-sonication as a rapid and effective approach for coating alumina on Li$_{1.2}$Ni$_{0.175}$Mn$_{0.525}$Co$_{0.1}$O$_2$ (0.5Li$_2$MnO$_3$·0.5LiNi$_{0.44}$Mn$_{0.31}$Co$_{0.25}$O$_2$) particles. Oxide integrity and morphology is maintained after the sonochemical process and subsequent heat-treatment. Energy dispersive spectroscopy (EDS) X-ray elemental maps show uniform coating of all secondary particles. ^{27}Al Magic Angle Spinning (MAS) NMR data confirm the presence of alumina and mainly indicate octahedral aluminum occupancy in a six-coordinate environment with oxygen. Full cells containing electrodes with the alumina-coated particles demonstrate lower initial impedance rise and better capacity retention during extended cycling to high voltages. However, the coating has a negligible effect on the voltage hysteresis and voltage fade behavior displayed by these oxides. The various data indicate that the pulsed sonochemical technique is a viable approach for coating oxide particles. The methodology described herein can easily be extended beyond alumina to include coatings such as AlF$_3$, MgO, and MgF$_2$.

© 2014 Elsevier B.V. All rights reserved.

1. Introduction

The ever-growing demand for higher energy storage densities has led to the development of novel electrode materials for lithium-ion cells. However, to attain these higher densities, the cells are cycled at high voltages (>4.5 V vs. Li/Li$^+$) beyond the stability window of conventional electrolytes [1–3]. At the positive electrode, the highly oxidizing conditions induce side reactions that trigger resistance rise, whereas at the negative electrode the highly reducing conditions induce changes in the solid electrolyte interphase (SEI) that enhance lithium trapping, thereby lowering cell capacity [4]. Stabilizing the electrode–electrolyte interfaces is critical to improving the performance, life, and safety of lithium-ion cells. A common approach to improving stability is through the use of electrolyte additives that create passivation layers at the interfaces [5–7]. An alternative approach is the use of electrode and/or active material coatings that provide a physical and/or chemical barrier to detrimental side reactions at the interface [8].

Metal oxides (MO$_x$, M = Mg, Zr, V, Zn, Al, Co, Sn) are among the most widely studied coating materials [9]; metal phosphates [10,11], metal fluorides [12], and metal oxyfluorides [13] coatings

* Corresponding author. Tel.: +1 630 252 4332.
  E-mail address: abraham@anl.gov (D.P. Abraham).

are also reported in the research literature. Of the various materials studied, coatings based on alumina are shown to have a significant impact on cell performance. These coatings have been studied on $LiMn_2O_4$, $LiCoO_2$, Fe_3O_4, graphite, and silicon materials and are credited with suppressing phase transitions, lowering transition metal dissolution, and reducing impedance rise during cycling.

Conventional coatings are applied via wet-chemical methods that use aqueous or non-aqueous solvents and employ multiple complex steps [14–16]; more recently, dry-coating techniques are gaining prominence because of their relative simplicity [17]. Another widely used technique, atomic layer deposition (ALD), has been broadly applied to create conformal, ultrathin, coatings on both positive and negative electrodes/materials [18–22]. In this article, we report a sonochemical approach for application of alumina coatings on lithium- and manganese-rich layered oxides, which are attractive candidates for high energy cells because of their high capacities (>250 Ah kg^{-1}).

Sonochemistry refers to chemical reactions caused by acoustic cavitation [23]. Acoustic cavitation is the phenomenon by which intense ultrasonic waves induce the formation, growth, and subsequent collapse of micro-bubbles in liquid [24] leading to the formation of free radicals [25]. For example, the sonolysis of a water molecule into ·OH and ·H radicals results in oxidation, reduction, dissolution, and decomposition reactions in the reaction vessel [26]. Near a solid surface, the collapse produces physical effects such as acoustic streaming [26], microjets [27], and shock waves [28]. Cavitation-induced sonochemistry creates a unique interaction between energy and matter [29], with hot spots inside the bubbles of ~ 5000 K, pressures of ~ 1000 bar, and heating and cooling rates of $>10^{10}$ K s^{-1}. These extraordinary conditions permit access to a range of chemical reaction space, normally not accessible, that allows for the synthesis of a wide variety of unusual nanostructured materials [29].

In previous articles, we have demonstrated the use of a continuous-sonochemical approach for surface coatings of oxides and carbon materials [30–35]. This approach is, however, unsuitable for surface modification of oxide particles typically used in lithium-ion cells because the extreme conditions induced by cavitation severely alters their secondary particle/primary particle architecture. Herein, we demonstrate a pulsed-sonochemical approach for coating alumina on $Li_{1.2}Ni_{0.175}Mn_{0.525}Co_{0.1}O_2$ ($0.5Li_2MnO_3 \cdot 0.5LiNi_{0.44}Mn_{0.31}Co_{0.25}O_2$) particles that maintain their pristine morphology after the process. In this approach, the ultrasonic energy is delivered in pulsed cycles (4 s ON, 4 s OFF) for 15 min. The pulsed nature of the process facilitates percolation of reactant solutions into the secondary particle interior thus enabling the coating of individual primary particles.

The pulsed-sonochemical approach has been employed previously for various purposes including the synthesis of copper oxide and tin oxide nanoparticles [36,37]. Herein, we report on the use of pulsed sonication for coating oxide particles for battery applications. Electrodes prepared from the alumina-coated oxide particles have been examined in cells with lithium- and graphite-based counter electrodes. Our investigations reveal that pulsed sonochemistry is a novel and rapid approach for the application of nanoparticulate coatings on oxide particles. Cells containing the coated particles demonstrate lower impedance rise and better capacity retention during extended cycling at elevated voltages.

2. Experimental

The pristine $Li_{1.2}Ni_{0.175}Mn_{0.525}Co_{0.1}O_2$ (henceforth referred to as LMR-NMC) material is prepared by a solid-state reaction process according to the protocol described in Ref. [38]. The sonochemical coatings are applied in the following manner. First, the oxide is

dispersed in deionized water by pulsed sonication to clean and activate the particle surfaces. The ultrasonic energy is delivered at 40% intensity (maximum frequency, 20 kHz) during this process to preserve the secondary particle morphology; higher frequency values promote particle damage as shown later. Then the precursor solution, aqueous $Al(NO_3)_3 \cdot 9H_2O$, is added to the pre-dispersed LMR-NMC aqueous slurry. The pH of the reaction mixture is maintained slightly basic ($\sim$pH 8) by simultaneous drop-wise addition of dilute NH_4OH solution, which is a precipitating and chelating agent (Fig. 1). The pulsed sonication continues throughout the entire precipitation process with the ultrasonic energy being delivered in pulsed cycles (programmable 4 s ON and 4 s OFF times) for a total processing time of 15 min.

After pulsed sonication, the product is centrifuged at 4000 rpm and washed twice with deionized water to remove by-products, such as ammonium nitrate. The resulting material is dried at 110 °C and then heat-treated at 500 °C for 2 h in air to obtain the final product. The reaction chemistry during the sonochemical process is detailed in Fig. 1; the particles are initially coated with aluminum hydroxide that is converted to aluminum oxide during the final heat-treatment process. In this work, we use 2 wt% $Al(NO_3)_3 \cdot 9H_2O$ precursor and 98 wt% LMR–NMC powder pre-dispersed in water; precipitation with excess NH_4OH solution creates $Al(OH)_3$, which is heated to form the alumina. Because the
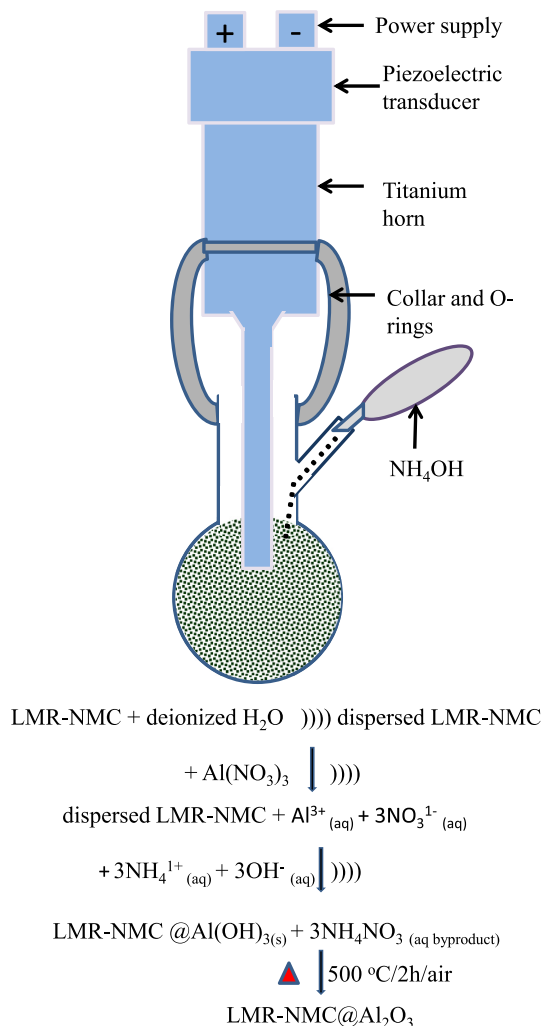

LMR-NMC + deionized H_2O)))) dispersed LMR-NMC

$+ Al(NO_3)_3$ ⎮))))

dispersed LMR-NMC + $Al^{3+}_{(aq)}$ + $3NO_3^{1-}{}_{(aq)}$

$+ 3NH_4^{1+}{}_{(aq)}$ + $3OH^-{}_{(aq)}$ ⎮))))

LMR-NMC @$Al(OH)_{3(s)}$ + $3NH_4NO_3$ (aq byproduct)

▲ ⎮ 500 °C/2h/air

LMR-NMC@Al_2O_3

Fig. 1. Pulsed sonochemical reaction set up and reaction pathway. The)))) symbol represents the pulsed sonication process.

Al(NO$_3$)$_3$·9H$_2$O (Mol. wt. = 375.13 g mol^{-1}) converts to Al$_2$O$_3$ (Mol. wt. = 101.96 g mol^{-1}), the 2 wt% precursor yields ~0.005 g of Al$_2$O$_3$ on ~0.98 g of the LMR–NMC powder surface, i.e., an estimated 0.5 wt% alumina is present on the oxide particles.

The alumina-coated oxide particles are characterized by various techniques that include scanning electron microscopy (SEM), X-ray diffraction (XRD), and nuclear magnetic resonance (NMR) spectroscopy. SEM imaging is conducted on a field emission scanning electron microscope (JEOL JSM7500F) equipped with a Thermo Fisher energy dispersive X-ray analysis unit. Powder X-ray diffraction patterns are collected with a Bruker D8 Advance diffractometer (CuK$_\alpha$ radiation) at a scan rate of 0.33° 2θ min^{-1}.

The Magic Angle Spinning (MAS) NMR data are acquired on oxide powder samples. The ^{27}Al MAS NMR experiments are performed on a Bruker Avance III 500 MHz spectrometer (11.7 T superconducting magnet) with a 2.5 mm MAS probe operating at 28 kHz spinning speed. The spectra are referenced to 1 M Al(NO$_3$)$_3$ at 0 ppm and single pulse experiments are performed with a pulse width of 1.0 μs and a recycle delay of 1 s. ^{1}H MAS NMR experiments are acquired on a Bruker Avance III 300 MHz spectrometer (7.05 T) with a 1.3 mm MAS probe at a spinning speed of 65 kHz. All spectra are referenced to TMS at 0 ppm and a single pulse experiment is used with a π/2 pulse width of 1.4 μs and a recycle delay of 1 s. A background spectrum is acquired under the same conditions and parameters and is subtracted from the actual data for the ^{1}H MAS NMR experiments.

For electrochemical cycling experiments, the positive electrodes comprise a coating of oxide (as-prepared or alumina-coated), carbon black and PVdF in the 82:8:10 ratio on an Al foil current collector; the oxide loading density is ~4.3 mg cm^{-2}. The negative electrode is either Li-metal (half-cell) or a graphite-based electrode (full-cell) that comprises a coating of graphite (Philips 66, A12), Timcal C45 carbon, and PVdF (Kureha KF9300) in the 92:2:6 ratio on a Cu foil current collector; the graphite loading density is ~5.2 mg cm^{-2}. All cells contain a polypropylene–polyethylene–polypropylene trilayer (Celgard 2325) separator, and an EC:EMC (3:7 by wt.) + 1.2 M LiPF$_6$ electrolyte (also known as "Gen2" from Tomiyama Chemical Industry, Japan); the moisture content of the electrolyte is ~20 ppm. Electrochemical cycling experiments are conducted with 1.6 cm^2 area electrodes in 2032-type coin cells. These cells are assembled in an Ar-atmosphere glove box and galvanostatically cycled within a constant temperature oven held at 30 °C.

The formation cycling of the positive electrode half-cells followed two different protocols. Our baseline protocol consists of cycling the cells in the 2–4.6 V voltage window with a 15 mA g^{-1} current, followed by extended cycling with a 150 mA g^{-1} current. Our altered protocol consists of cycling the cells sequentially in the 2.2–4.4 V, 2.2–4.5 V, 2.2–4.6 V and 2.2–4.7 V voltage windows with a 15 mA g^{-1} current: similar "window-opening" protocols have been shown to enhance capacities and cycling stabilities of cells containing various lithium-rich layered oxides [39–42]. Extended cycling of these cells is conducted in the 2.2–4.7 voltage window with a 75 mA g^{-1} current.

Because the window-opening experiments on half cells provided higher capacities, the full cells are cycled sequentially in the 2.2–4.3 V, 2.2–4.4 V, 2.2–4.5 V and 2.2–4.6 V voltage windows with a 15 mA (g oxide)$^{-1}$ current, followed by extended cycling with a 75 mA (g oxide)$^{-1}$ current. The extended cycling is interrupted periodically to obtain capacity and AC impedance data. The capacity data are obtained with a 15 mA (g oxide)$^{-1}$ current because the smaller current reduces impedance effects in the cycling plots. The AC impedance data are collected after the cells are charged to 3.75 V and held at that voltage for more than 12 h; the data are obtained at 30 °C in the 100 kHz to 10 mHz frequency range, with a 10 mV perturbation around the open-circuit voltage [4].

3. Results

3.1. Oxide particle and coating characterization

XRD patterns from the oxide powders are similar to those reported in previous articles [4,38] and are, therefore, not shown here. Most diffraction peaks in the patterns can be indexed based on the α-NaFeO$_2$ (R-3m) structure; a set of small, relatively broad peaks in the 2θ = 22°–25° range are characteristic of cation ordering in the transition metal (TM) layers, as occurs between the lithium and manganese ions in Li$_2$MnO$_3$ [43,44]. No discernible changes are induced by the alumina coatings. SEM images of the coated and uncoated oxides are also very similar. The images show 10–20 μm size secondary particles that consist of dense, plate-like, sub-micron size primary particles. The secondary particle morphology and architecture is preserved during the pulsed sonication process. In contrast, the morphology is altered significantly if continuous sonication is used, or if the ultrasonic energy is delivered at higher than the 40% threshold intensity used in our coating process (Fig. 2). An alumina coating is indicated by X-ray elemental maps generated by EDS. In Fig. 3, the Ni and O signals arise primarily from the oxide; the Al signal distribution is similar indicating that the particles are covered by the coating.

The presence of alumina is further confirmed by ^{27}Al and ^{1}H solid-state NMR experiments that probe changes in the coordination and local environments of aluminum and proton species immediately after sonication, and following the final heat-treatment. Although it is considered a bulk technique, multinuclear NMR analysis can provide information on surface species such as coatings. ^{27}Al MAS NMR has been previously used on various cathode materials, such as aluminum-doped LiCoO$_2$ (LiAl$_x$Co$_{1-x}$O$_2$), Al$_2$O$_3$-coated LiCoO$_2$, LiAl$_x$Ni$_{1-x}$O$_2$ and AlF$_3$-coated Li[Li$_{1/9}$Ni$_{1/3}$Mn$_{5/9}$]O$_2$, to obtain information on the local environment of Al atoms both on the oxide surface (coating) and in the bulk (lattice) [45–49]. Six-coordinate aluminum environments in Al$_2$O$_3$ and Al(OH)$_3$ resonate between 0 and 10 ppm whereas 4- and 5-coordinated aluminum atoms of aluminum oxides show distinct ^{27}Al NMR peaks within 50–80 and 30 ppm regions, respectively [50]. Studies on LiAl$_x$Co$_{1-x}$O$_2$ have shown a distribution of lattice aluminum chemical shifts between 30 and 60 ppm with varying the cobalt contents [45,47].

Fig. 4 displays the ^{27}Al MAS data from the as-sonicated and heat-treated materials. The as-sonicated material shows a single peak centered at 6.7 ppm that can be assigned as an octahedral aluminum hydroxide environment (which is confirmed by ^{1}H NMR) [50]. After heat-treatment, this 6-coordinate aluminum peak shows a slight broadening and a shift to 7.4 ppm. A weak broad signal covering the 25–100 ppm region is also observed. This broad feature indicates a distribution of different aluminum environments and is most likely due to 5- and 4-coordinate aluminum sites formed during heat treatment either on the surface (aluminum oxide species [50]) and/or at the coating-oxide interface. The latter case may include aluminum atoms coordinated to lattice lithium and cobalt sites via oxygen atoms as previous studies on LiAlO$_2$ and LiAl$_x$Co$_{1-x}$O$_2$ samples show a wide range of peak distributions in 15–70 ppm region [45–47]. Note that any lattice aluminum in the vicinity of paramagnetic metal centers (Ni, Mn) should give ^{27}Al resonances at higher frequencies; this higher frequency range is not covered in this study.

The ^{27}Al data are complemented by ^{1}H MAS NMR data, acquired to confirm the identity of the surface 6-coordinate Al species, before and after heat-treatment. As seen in Fig. 5, the ^{1}H MAS data of the as-sonicated sample shows three major peaks centered at 0.2, 2.8 and 6.0 ppm. By comparing with literature shift values [50], these environments can be assigned as protons of NH$_4^+$ impurities
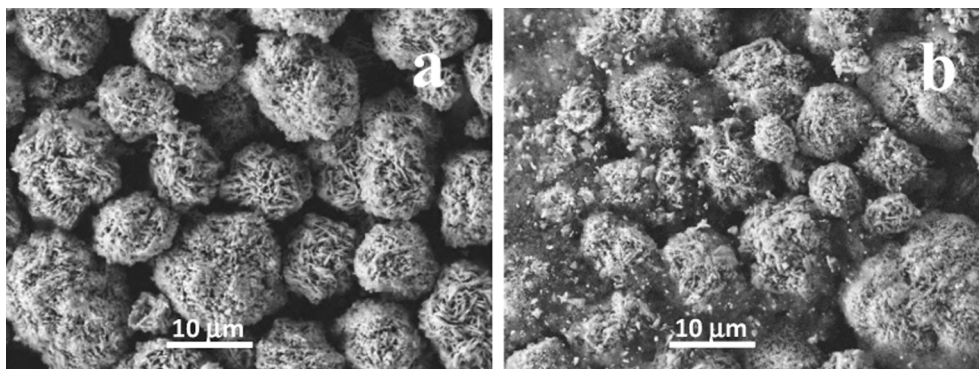
Fig. 2. SEM images of oxide particles coated by a) pulsed sonication and b) continuous sonication for 15 min at 40% ultrasonic intensity. Changes/damage to the oxide particle morphology is evident in (b).

from the synthesis solution, $Al(OH)_3$ species, and adsorbed water, respectively. The identity of the minor impurity/artifact peak appearing at -10 ppm is not known. Heat-treatment results in the complete removal of water and hydrogen impurities and further confirms conversion of the $Al(OH)_3$ species to aluminum oxides as shown in Fig. 1.

3.2. Electrochemical characterization in half and full cells

Fig. 6a and b shows the first two charge–discharge plots, obtained with a 15 mA g^{-1} current, from half cells containing electrodes with the pristine and alumina-coated oxides. For both cells a plateau at $\sim$4.4 V is seen during the first charge cycle. This plateau is attributed to electrochemical activation of the Li_2MnO_3 component and is typically associated with structural changes and loss of oxygen from the oxide [51,52]. For the pristine electrode, the first cycle charge and discharge capacities (in mAh g^{-1}) are 261 and 199, respectively, yielding a 76% coulombic efficiency; the corresponding values for the coated electrode are 273 and 222, respectively,

yielding an 81% coulombic efficiency. For the 2nd cycle, the discharge capacities (in mAh g^{-1}) are slightly higher, 202 and 231, and the coulombic efficiencies are significantly higher, 99.3% and 99.7%, for the pristine and coated electrode, respectively.

Fig. 6c shows a discharge capacity vs. cycle number plot obtained with a 150 mA g^{-1} current. For the pristine electrode the discharge capacities remain relatively stable at $\sim$140 mAh g^{-1} over the 50 cycles; the corresponding value for the coated electrode is 170 mAh g^{-1}. It is evident that the performance of the alumina-coated electrode is better at both low and high currents; the significant difference at the higher current indicates lower impedance for the coated electrode.

Because the capacity values obtained with our baseline protocol are lower than expected, we employed the "window-opening" protocol described earlier. A typical capacity–voltage plot, obtained with a 15 mA g^{-1} current, for the pristine electrode is shown in Fig. 7a. The charge//discharge capacities (in mAh g^{-1}) for the various cycles are as follows: 117//105 (2.2–4.4 V), 214//181 (2.2–4.5 V), 243//230 (2.2–4.6 V), and 254//245 (2.2–4.7 V). The
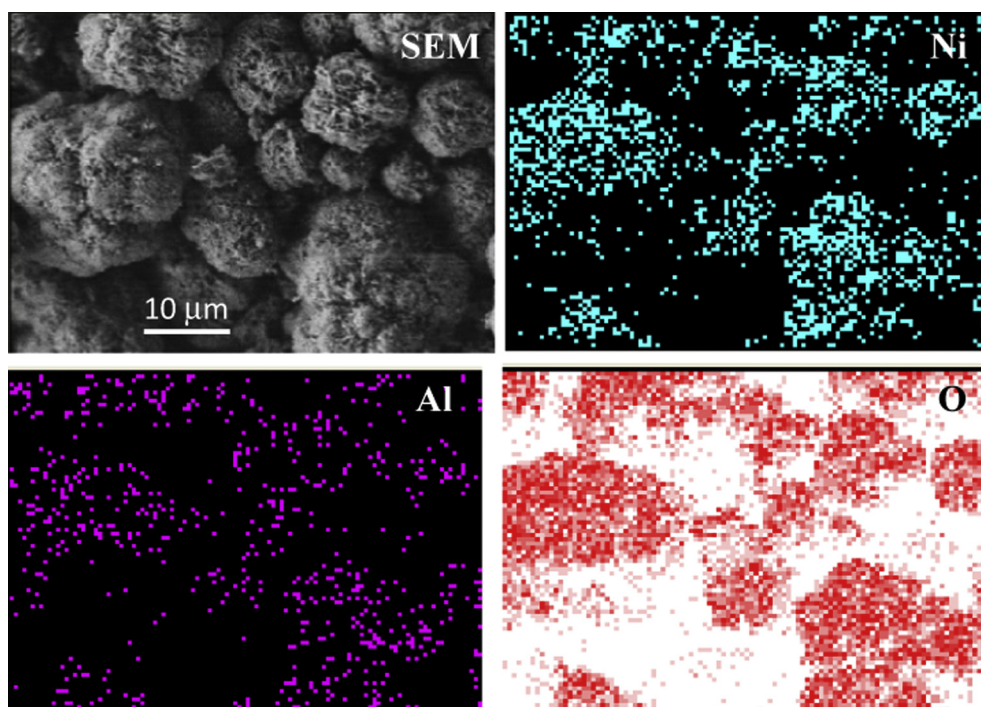

Fig. 3. Scanning electron microscopy (SEM) image and corresponding nickel, aluminum and oxygen, energy dispersive X-ray element maps from alumina-coated LMR–NMC oxide particles.
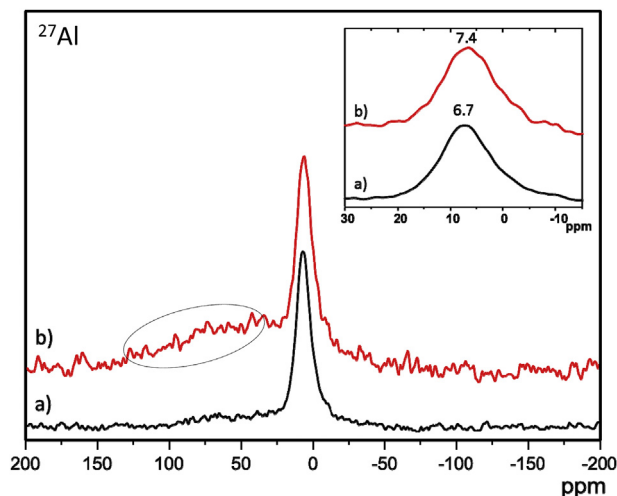
Fig. 4. ^{27}Al MAS NMR of oxide particles that are (a) as-coated, and (b) heat-treated at 500 °C, 2 h. The inset is a magnified view of the spectra showing six-coordinate aluminum environments. The broad feature enveloped by the dashed oval is probably from five- and four-coordinate aluminum sites formed during heat treatment.

corresponding charge//discharge capacities (mAh g^{-1}) for the coated sample are similar: 113//106 (2.2–4.4 V), 216//187 (2.2–4.5 V), 249//239 (2.2–4.6 V), and 261//251 (2.2–4.7 V). For both pristine and coated electrode cells, partial plateaus are seen in the 2.2–4.4 V, 2.2–4.5 V and 2.2–4.6 V cycles, indicating gradual activation of the oxide particles. After formation, the cells are cycled with a 75 mA g^{-1} current. The resulting discharge capacity vs. cycle number plot (see Fig. 7b) shows that the cycling behavior of half cells with the pristine and coated electrode is similar. That is, following the gradual activation protocol no obvious advantage is evident for the coated electrode.

Many Li-intercalating oxides display a decrease in the charge and discharge voltages during cycling [53–56]. This phenomenon, referred to as "voltage fade" causes a continuous decrease in the cell's energy output. Fig. 8 shows that the alumina coating, applied by our pulsed sonication technique, has a negligible effect on voltage fade. The charge–discharge plots, after formation cycles and after 50 cycles, are very similar for cells with the pristine and alumina-coated oxides. Also, the coating has minimal effect on the voltage hysteresis, which is the difference between the charge and discharge plots for any given cycle [57,58]. The voltage hysteresis arises from differences in lithium site occupancy during charge and discharge; this site occupancy is unaffected by the coating, which
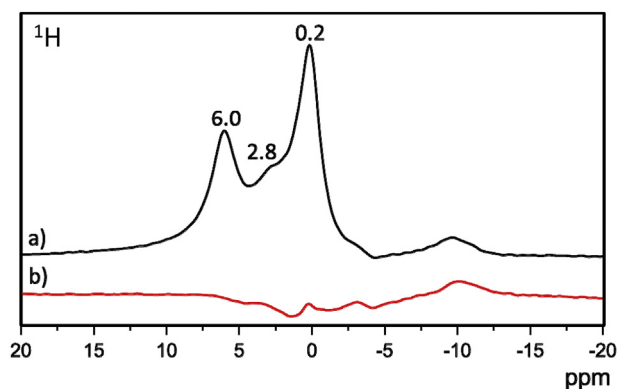

Fig. 5. ^1H MAS NMR of oxide particles that are (a) as-coated, and (b) heat-treated at 500 °C, 2 h. A background spectrum acquired with an empty rotor using the same experimental parameters is subtracted from both spectra.

indicates that voltage hysteresis is a characteristic of the oxide bulk. The voltage fade is caused by irreversible, structural changes in the oxide; negligible effect of the coating indicates that this fade is also determined by the oxide bulk.

The formation cycles on our full cells follow the "window-opening" protocol. A representative capacity–voltage plot, obtained with a 15 mA (g oxide)$^{-1}$ current, for the coated electrode is shown in Fig. 9a. The charge//discharge capacities (in mAh g^{-1}) for the various cycles are as follows: 131//98 (2.2–4.3 V), 203//181 (2.2–4.4 V), 238//227 (2.2–4.5 V), and 250//244 (2.2–4.6 V). The capacities for the pristine electrode cells were qualitatively similar but slightly lower. The higher inefficiency in the 2.2–4.3 V cycle is partially related to lithium trapping in the SEI during the first graphite-lithiation cycle.
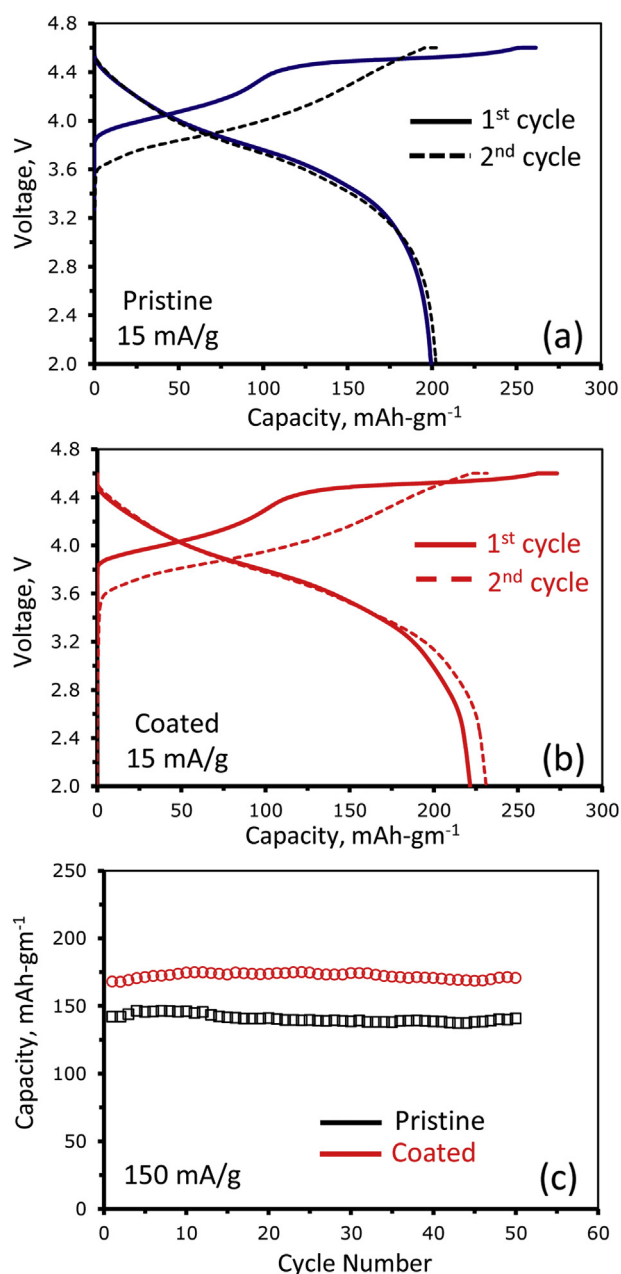

Fig. 6. First two cycles, obtained with a 15 mA g^{-1} current, from half cells containing the (a) pristine-oxide, and (b) alumina-coated oxide electrodes, respectively. (c) Discharge capacity vs. cycle number plot obtained with a 150 mA g^{-1} current in the 2–4.6 V range.
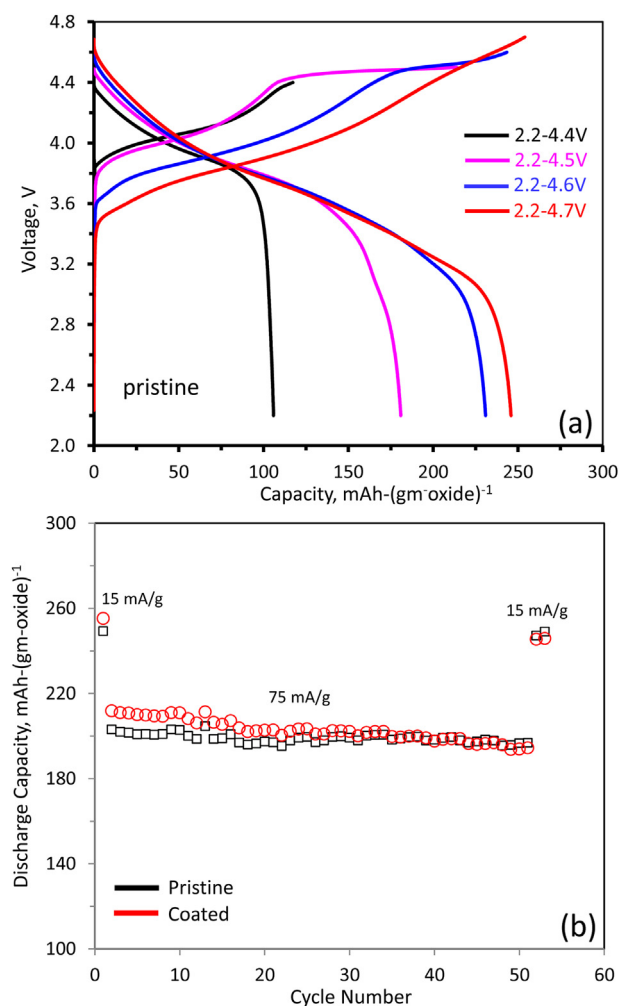
Fig. 7. (a) Capacity—voltage plots from the "window-opening" cycling protocol for a half-cell containing a pristine electrode cycled with a 15 mA g^{-1} current. (b) Discharge capacity vs. cycle number plots for cells with the pristine and coated electrodes cycled in the 2.2—4.7 V range.

Fig. 8. Capacity—voltage plots (2—4.7 V, 15 mA g^{-1}), from half-cells containing the pristine and coated electrodes, after formation cycling and after fifty 2.2—4.7 V cycles. The alumina coating has negligible effect on the oxide's voltage hysteresis and voltage fade characteristics.

Fig. 9. (a) Capacity—voltage plots from the "window-opening" cycling protocol from a full-cell containing an alumina-coated electrode cycled with a 15 mA (g oxide)$^{-1}$ current. (b) Discharge capacity vs. cycle number plots for cells with the pristine and coated electrodes cycled in the 2.2—4.6 V range.

The discharge capacity data, on extended cycling with a 75 mA (g oxide)$^{-1}$ current, is shown in Fig. 9b. It is evident that the discharge capacity of the alumina-coated electrode cell is higher than that of the pristine electrode cell, especially at the higher current. The discharge capacity fade, after a hundred 2.2—4.6 V cycles, for the pristine electrode cell, is 9% and 17%, respectively, at the high and low currents; the corresponding values for the coated electrode cell are 6% and 15%. That is, the rate of capacity fade is marginally lower for cells with the alumina coated electrode.

Distinct differences are, however, observed in the AC impedance spectra (see Fig. 10) from full-cells with the alumina-coated and pristine electrodes; the spectra include contributions from all cell components. Each spectrum is typical of LMR—NMC//graphite full cells [4,21], and includes (i) two major arcs in the 10 kHz to ~1 Hz range, which are generally associated with charge transport across particle—particle and particle—electrolyte interfaces; and (ii) a Warburg impedance tail at frequencies <1 Hz, which is associated with bulk diffusional effects in the cell, including diffusion of lithium within the electrode active materials [59]. Fig. 10a and b contains cell data after formation cycling and after one hundred 2.2—4.6 V cycles, respectively — it is evident that the alumina-coated cell has lower initial impedance and a significantly smaller impedance rise after extended cycling. The only difference between
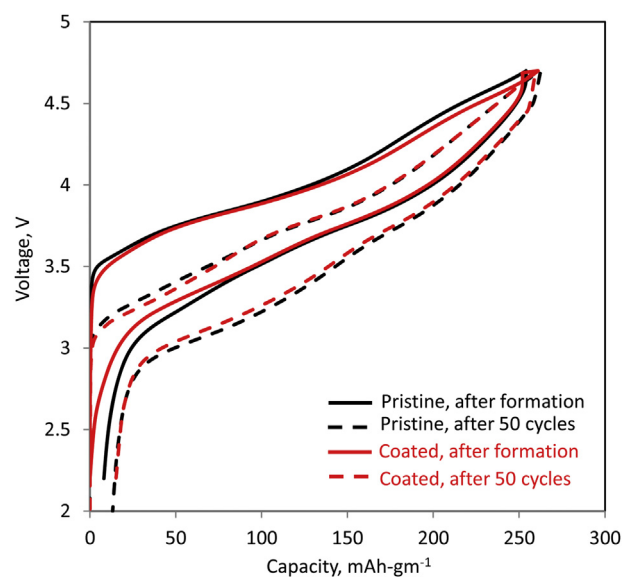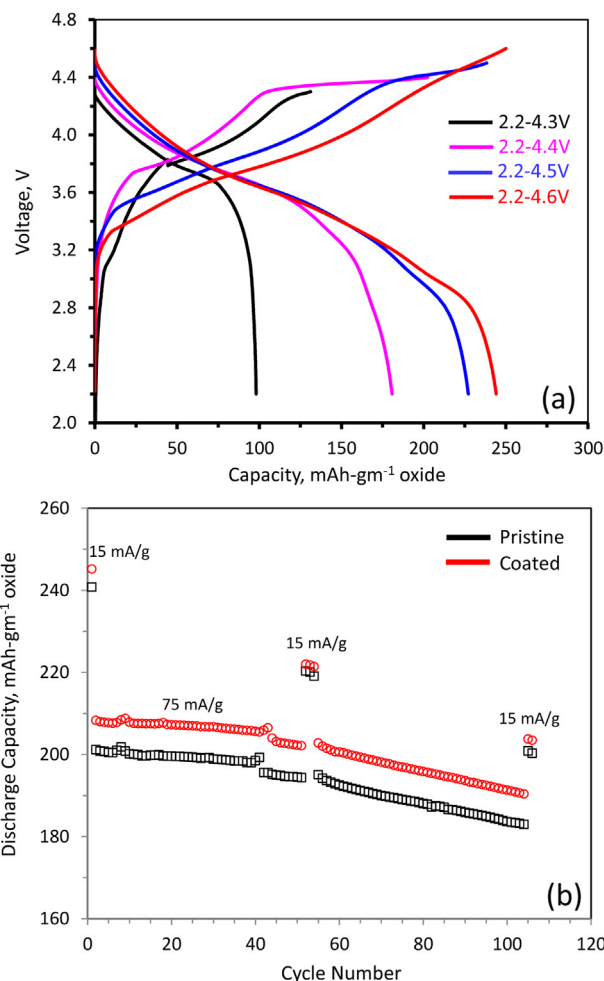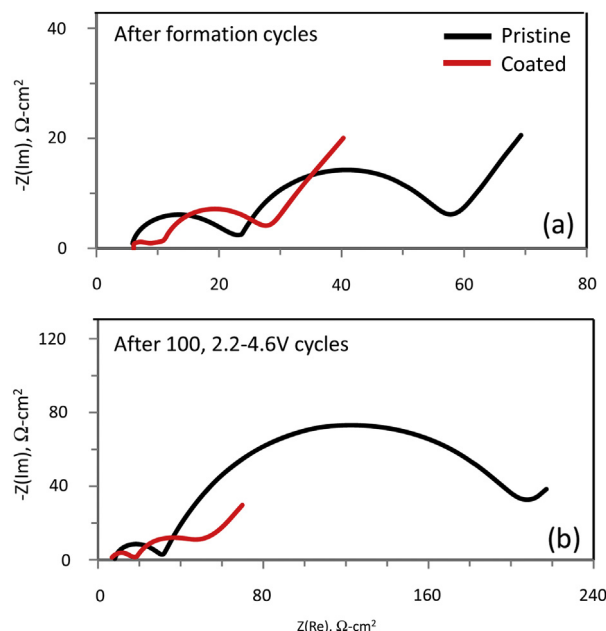
Fig. 10. AC impedance spectra from full cells with the pristine and alumina-coated electrodes: (a) after formation cycling, and b) after 100, 2.2–4.6 V cycles. The data are obtained in the 100 kHz to 0.01 Hz frequency range, at 30 °C and at a full cell voltage of 3.75 V.

the cells is the alumina-coating on the oxide particles − we may thereby conclude that the alumina coating reduces full cell impedance by lowering impedance at the positive electrode.

4. Discussion

Alumina coatings can be applied by various techniques including sol−gel, solid-state, dry-coating, atomic layer deposition (ALD), electrophoresis deposition (EPD) [60] and electrolytic deposition (ED) [61] techniques. Each technique has its own advantages and disadvantages. For example, the ALD technique can be used to generate conformal, ultrathin coatings on oxide particles and electrodes, but process scalability is yet to be demonstrated. Sol−gel based methods provide highly effective coatings but often require large quantities of solvents, multiple steps and long processing times. Dry-coating techniques, involving homogenizer-mixing followed by heat-treatment, are relatively simple but could induce changes in the secondary/primary architecture of battery oxides.

Our pulsed-sonication technique provides an alternative approach − a rapid and effective method for uniform coating of secondary particles with $Al(OH)_3$, which is converted to alumina during subsequent heat-treatment. The NMR data indicate the presence of aluminum−oxygen bonds at the oxide surface, and some Al migration into the oxide bulk. The strong Al−O bonds at the oxide surface could reduce the outward diffusion of oxygen vacancies thereby reducing irreversibility during the first oxide-activation cycle [42]. The possible formation of a $LiAl_xM_{(1−x)}O_2$ (M = Ni, Co, Mn) interphase [62] could reduce reactivity with the electrolyte and minimize the dissolution of transition metal elements, as suggested by Verdier et al. for alumina-coated $LiCoO_2$ [63].

The smaller impedance for the alumina-coated sample, after formation cycling and after extended cycling, is a prominent feature of our data. From kinetic Monte Carlo simulations Hao and Wolverton [64] report that the diffusivity of interstitial Li in amorphous α-Al_2O_3 coatings is very low ($D = 2.7 \times 10^{-14}$ m^2 s^{-1} at 600 K). Such low values would increase (not decrease) interfacial impedances. On the other hand, using ab initio molecular dynamics

simulations, Jung and Han [65] indicate that lithiation of Al_2O_3 coatings proceeds until a thermodynamically stable phase ($Li_{3.4}Al_2O_3$) forms. Lithium ions in this optimal composition diffuse four orders of magnitude faster than ions in Al_2O_3 with low Li concentrations. In a similar manner, the low impedances in our data may indicate the formation of Li-rich alumina phases, and/or faster diffusion through a $LiAl_xM_{(1−x)}O_2$ (M = Ni, Co, Mn) solid solution, at the oxide-electrolyte interface.

The alumina presence may also reduce the preferential segregation of Ni atoms to the oxide particle surface and boundaries reported by Gu et al. [66]. The authors concluded that preferential segregation of Ni ions to the particle surface is observed when the surface is terminated with a mix of cations and anions; such segregation is not observed for surfaces terminated with a transition-metal layer. Boulineau et al. also showed Ni segregation to $Li_{1.2}Mn_{0.6}Ni_{0.18}Mg_{0.01}O_2$ surfaces upon cycling, which results from Mn migration from the surface to the particle bulk [67]. Such surface structural transformations can affect the diffusion of lithium ions; for instance, the generation of a $Li_{1−x}Ni_xO$ layer on $LiNi_{0.8}Co_{0.2}O_2$ particle surfaces is known to impede lithium motion [68,69]. Termination of surfaces with aluminum from the alumina may minimize Ni atom segregation to the oxide particle surface, and thereby reduce impedance growth on extended cycling.

The enhanced capacity observed with our "window-opening" cycling protocol is similar to the effects reported previously. From transmission electron microscopy (TEM) studies, Ito et al. [70] determined that the standard galvanostatic cycling protocol induces micro-crack formation and crystal periodicity distortion because of oxygen loss from the oxide surface; the gradual activation protocol suppressed formation of these defects. Nakahara et al. [71] showed that stepwise cycling suppressed oxygen release from the oxide lattice during the first charge of graphite−$Li_{1.26}Mn_{0.52-}$ $Fe_{0.22}O_2$ full cells. Similarly, the enhanced capacity of cells with alumina-coated electrodes may result from the strong Al−O bonds which reduce oxygen evolution and, therefore, damage at the oxide surface. The reduction of oxygen evolution would also improve the safety characteristics of the oxide, as described in previous studies. Further studies are underway to determine optimal alumina and lithium aluminate concentrations and distributions for maximum improvements in cell performance, life and safety.

5. Conclusions

A pulsed-sonochemical approach is used to coat alumina on $Li_{1.2}Ni_{0.175}Mn_{0.525}Co_{0.1}O_2$ ($0.5Li_2MnO_3 \cdot 0.5LiNi_{0.44}Mn_{0.31}Co_{0.25}O_2$) particles. The pulsed-approach uniformly coats the oxide while maintaining its secondary particle/primary particle architecture, unlike continuous sonication processes that promote particle damage. The alumina coating is indicated by EDS X-ray elemental maps and confirmed by ^{27}Al MAS NMR data which are consistent with a 6-coordinate aluminum-oxygen environment. Standard 2−4.6 V galvanostatic cycling data in lithium-metal counter-electrode cells show that the performance of the alumina-coated electrode is better than that of the pristine electrode, both at low and high rates. However, the performance is similar for both electrodes when a "voltage window-opening" protocol is employed during the initial activation cycles. Furthermore, the alumina coating has a negligible effect on the voltage hysteresis and the voltage fade behavior displayed by these oxides.

When cycled with graphite-based negative electrodes, cells with the alumina-coated electrode have lower initial impedance, and a significantly smaller impedance rise after one hundred cycles, compared to the pristine electrode cell. The discharge capacity of the alumina-coated electrode cell is also higher than that of the pristine electrode cell, probably because of its lower impedance. It

is likely that the alumina forms a partial solid solution at the oxide surface to create, for example, a lithium aluminate layer, thereby stabilizing and reducing deleterious reactions and impedance at the oxide–electrolyte interface. Detailed studies are underway to determine optimal coating and processing conditions that enhance material performance and cell life.

Acknowledgments

References

[1] T. Ohzuku, Y. Makimura, Chem. Lett. 30 (2001) 744.
[2] Z. Lu, L.Y. Beaulieu, R.A. Donaberger, C.L. Thomas, J.R. Dahn, J. Electrochem. Soc. 149 (2002) A778.
[3] M.M. Thackeray, C.S. Johnson, J.T. Vaughey, S.A. Hackney, J. Mater. Chem. 15 (2004) 2257.
[4] Y. Li, M. Bettge, B. Polzin, Y. Zhu, M. Balasubramanian, D.P. Abraham, J. Electrochem. Soc. 160 (2013) A3006.
[5] S.S. Zhang, J. Power Sources 162 (2006) 1379.
[6] Y. Zhu, Y. Li, M. Bettge, D.P. Abraham, J. Electrochem. Soc. 159 (2012) A2109.
[7] Y. Zhu, M.D. Casselman, Y. Li, A. Wei, D.P. Abraham, J. Power Sources 246 (2014) 184.
[8] K.T. Lee, S. Jeong, J. Cho, Acc. Chem. Res. 46 (2013) 1161.
[9] J. Cho, Y.J. Kim, B. Park, Chem. Mater. 12 (2000) 3788.
[10] J. Cho, Y.-W. Kim, B. Kim, J.-G. Lee, B. Park, Angew. Chem. Int. Ed. 42 (2003) 1618.
[11] A.T. Appapillai, A.N. Mansour, J. Cho, Y. Shao-Horn, Chem. Mater. 19 (2007) 5748.
[12] S.-U. Woo, C.S. Yoon, K. Amine, I. Belharouak, Y.-K. Sun, J. Electrochem. Soc. 154 (2007) A1005.
[13] K.S. Lee, S.T. Myung, K. Amine, H. Yashiro, Y.K. Sun, J. Mater. Chem. 19 (2009) 1995.
[14] Y. Kim, J. Cho, J. Electrochem. Soc. 154 (2007) A495.
[15] H. Omanda, T. Brousse, C. Marhic, D.M. Schleich, J. Electrochem. Soc. 151 (2004) A922.
[16] J. Liu, A. Manthiram, J. Electrochem. Soc. 156 (2009) A833.
[17] Y. Cho, J. Cho, J. Electrochem. Soc. 157 (2010) A625.
[18] I.D. Scott, Y.S. Jung, A.S. Cavanagh, Y. Yan, A.C. Dillon, S.M. George, S.-H. Lee, Nano Lett. 11 (2011) 414.
[19] Y.S. Jung, P. Lu, A.S. Cavanagh, C. Ban, G.-H. Kim, S.-H. Lee, S.M. George, S.J. Harris, A.C. Dillon, Adv. Energy Mater. 3 (2012) 213.
[20] Y.S. Jung, A.S. Cavanagh, Y. Yan, S.M. George, A. Manthiram, J. Electrochem. Soc. 158 (2011) A1298.
[21] M. Bettge, Y. Li, B. Sankaran, N.D. Rago, T. Spila, R.T. Haasch, I. Petrov, D.P. Abraham, J. Power Sources 233 (2013) 346.
[22] X. Xiao, P. Lu, D. Ahn, Adv. Mater. 23 (2011) 3911.
[23] K.S. Suslick, L.A. Crum, in: M.J. Crocker (Ed.), Handbook of Acoustics, J. Wiley, New York, 1998. Ch. 23.
[24] T.J. Mason, Practical Sonochemistry: User's Guide to Applications in Chemistry and Chemical Engineering, E. Horwood, New York, 1991.
[25] K.S. Suslick, D.A. Hammerton, R.E. Cline, J. Am. Chem. Soc. 108 (1986) 5641.
[26] K.S. Suslick, Science 247 (1990) 1439.
[27] T.G. Leighton, The Acoustic Bubble, Academic Press, London, 1994.
[28] R. Pecha, B. Gompf, Phys. Rev. Lett. 84 (2000) 1328.
[29] J.H. Bang, K.S. Suslick, Adv. Mater. 22 (2010) 1039.
[30] V.G. Pol, D.N. Srivastava, O. Palchik, V. Palchik, M.A. Slifkin, A.M. Weiss, A. Gedanken, Langmuir 18 (2002) 3352.
[31] J.S. Gnanaraj, V.G. Pol, A. Gedanken, D. Aurbach, Electrochem. Commun. 5 (2003) 940.
[32] V.G. Pol, A. Gedanken, J. Calderon-Moreno, Chem. Mater. 15 (2003) 1111.
[33] V.G. Pol, M. Motiei, A. Gedanken, J. Calderon-Moreno, Y. Mastai, Chem. Mater. 15 (2003) 1378.
[34] V.G. Pol, O. Palchik, A. Gedanken, I. Felner, J. Phys. Chem. B 106 (2002) 9737.
[35] V.G. Pol, R. Reisfeld, A. Gedanken, Chem. Mater. 14 (2002) 3920.
[36] V. Mancier, A.-L. Daltin, D. Leclercq, Ultrason. Sonochem. 15 (2008) 157.
[37] J. Zhu, Z. Lu, S.T. Aruna, D. Aurbach, A. Gedanken, Chem. Mater. 12 (2000) 2557.
[38] S.-H. Kang, S.-H. Park, C.S. Johnson, K. Amine, J. Electrochem. Soc. 154 (2007) A268.
[39] A. Ito, D. Li, Y. Ohsawa, Y. Sato, J. Power Sources 183 (2008) 344.
[40] A. Watanabe, F. Matsumoto, M. Fukunishi, G. Kobayashi, A. Ito, M. Hatano, Y. Ohsawa, Y. Sato, Electrochemistry 80 (2012) 561.
[41] T. Ohzuku, M. Nagayama, K. Tsuji, K. Ariyoshi, J. Mater. Chem. 21 (2011) 10179.
[42] A. Bommel, L.J. Krause, J.R. Dahn, J. Electrochem. Soc. 158 (2011) A731.
[43] C.H. Lei, J.G. Wen, M. Sardela, J. Bareno, I. Petrov, S.-H. Kang, D.P. Abraham, J. Mater. Sci. 44 (2009) 5579.
[44] J. Bareño, C.H. Lei, J.G. Wen, S.-H. Kang, I. Petrov, D.P. Abraham, Adv. Mater. 22 (2010) 1122.
[45] E. Gaudin, F. Taulelle, R. Stoyanova, E. Zhecheva, R. Alcantara, P. Lavela, J.L. Tirado, J. Phys. Chem. B 105 (2001) 8081.
[46] Y. Lee, A.J. Woo, K.-S. Han, K.S. Ryu, D. Sohn, D. Kim, H. Lee, Electrochim. Acta 50 (2004) 491.
[47] N. Kosova, E. Devyatkina, A. Slobodyuk, V. Kaichev, Solid State Ionics 179 (2008) 1745.
[48] G.T.K. Fey, H.M. Hao, P. Muralidharan, T.P. Kumar, Y.D. Cho, J. Power Sources 163 (2006) 135.
[49] K.J. Rosina, M. Jiang, D. Zeng, E. Salager, A.S. Best, C.P. Grey, J. Mater. Chem. 22 (2012) 20602.
[50] K.J.D. MacKenzie, M.E. Smith, Multinuclear Solid-state NMR of Inorganic Materials, in: Pergamon Materials Series, vol. 6, Pergamon, Netherlands, 2002.
[51] A.R. Armstrong, M. Holzapfel, P. Novak, C.S. Johnson, S.-H. Kang, M.M. Thackeray, P.G. Bruce, J. Am. Chem. Soc. 128 (2006) 8694.
[52] M.M. Thackeray, S.-H. Kang, C.S. Johnson, J.T. Vaughey, R. Benedek, S.A. Hackney, J. Mater. Chem. 17 (2007) 3112.
[53] J.R. Croy, D. Kim, M. Balasubramanian, K. Gallagher, S.-H. Kang, M.M. Thackeray, J. Electrochem. Soc. 159 (2012) A781.
[54] B.J. Neudecker, R.A. Zuhr, J.D. Robertson, J.B. Bates, J. Electrochem. Soc. 145 (1998) 4160.
[55] D. Mohanty, S. Kalnaus, R.A. Meisner, K.J. Rhodes, J. Li, E.A. Payzant, D.L. Wood III, C. Daniel, J. Power Sources 229 (2013) 239.
[56] S.K. Martha, J. Nanda, Y. Kim, R.R. Unocic, S. Pannala, N.J. Dudney, J. Mater. Chem. A 1 (2013) 5587.
[57] M. Bettge, Y. Li, K. Gallagher, Y. Zhu, Q. Wu, W. Lu, I. Bloom, D.P. Abraham, J. Electrochem. Soc. 160 (2013) A2046.
[58] J.R. Croy, K.G. Gallagher, M. Balasubramanian, B.R. Long, M.M. Thackeray, J. Electrochem. Soc. 161 (2014) A318.
[59] D. Dees, E. Gunen, D. Abraham, A. Jansen, J. Prakash, J. Electrochem. Soc. 152 (2005) A1409.
[60] A.R. Boccaccini, U. Schindler, H.-G. Kruger, Mater. Lett. 51 (2001) 225.
[61] A.R. Boccaccini, I. Zhitomirsky, Curr. Opin. Solid State Mater. Sci. 6 (2002) 251.
[62] L. Daheron, R. Dedryvere, H. Martinez, D. Flahaut, M. Menetrier, C. Delmas, D. Gonbeau, Chem. Mater. 21 (2009) 5607.
[63] S. Verdier, L. Ouatani, R. Dedryvère, F. Bonhomme, P. Biensan, D. Gonbeau, J. Electrochem. Soc. 154 (2007) A1088.
[64] S. Hao, C. Wolverton, J. Phys. Chem. C 117 (2013) 8009.
[65] S.C. Jung, Y.-K. Han, J. Phys. Chem. Lett. 4 (2013) 2681.
[66] M. Gu, I. Belharouak, A. Genc, D. Wang, Z. Wang, K. Amine, F. Gao, G. Zhou, S. Thevuthasan, D.R. Baer, J.-G. Zhang, N.D. Browning, J. Liu, C. Wang, Nano Lett. 12 (2012) 5186.
[67] A. Boulineau, L. Simonin, J.-F. Colin, C. Bourbon, S. Patoux, Nano Lett. 13 (2013) 3857.
[68] D.P. Abraham, R.D. Twesten, M. Balasubramanian, I. Petrov, J. McBreen, K. Amine, Electrochem. Commun. 4 (2002) 620.
[69] D.P. Abraham, R.D. Twesten, M. Balasubramanian, J. Kropf, D. Fischer, J. McBreen, I. Petrov, K. Amine, J. Electrochem. Soc. 150 (2003) A1450.
[70] A. Ito, D. Li, Y. Sato, M. Arao, J. Power Sources 195 (2010) 567.
[71] K. Nakahara, M. Tabuchi, S. Kuroshima, A. Toda, K. Tanimoto, K. Nakano, J. Electrochem. Soc. 159 (2012) A1398.